CFD Modeling and Simulation of Clogging in Packed Beds with Nonaqueous Media

Arturo Ortiz-Arroyo, Faïçal Larachi, Bernard P. A. Grandjean, and Shantanu Roy
Chemical Engineering Dept., Laval University, Quebec, G1K 7P4, Canada

When liquids containing low concentrations of fine solid impurities are treated in packed-bed reactors, clogging develops and starts hampering the flow severely. This phenomenon, called deep-bed filtration, constitutes serious concern over hydrotreating or hydrocracking of bituminous sands in packed-bed reactors, in which such nonfilterable fines as native clay or incipient coke cause reactor dysfunction by clogging. A detailed k-fluid Eulerian 2-D transient computational-fluid dynamic (CFD) model was formulated to describe the space-time evolution of clogging patterns developing in deep-bed filtration of the liquids. A local formulation of the macroscopic logarithmic filtration law is proposed, as well as a geometrical model for the effective specific surface area of momentum exchange. Both mono- and multiple-layer deposition mechanisms were accounted for by including appropriate filter coefficient formulations. Transient, 2-D axisymmetrical simulations were benchmarked using experimental results and observations of Narayan et al. (1997) of the carbon-black contaminated kerosene flow through packed beds. Comparing the simulations and experiments showed that CFD is useful for the quantitative description of packed-bed clogging.

Introduction

Trickle-bed reactors (TBRs), which are catalytic fixed beds contacted by cocurrent downward gas-liquid flows, host a variety of gas-liquid-solid catalytic reactions especially in the petroleum and petrochemical industries. The economic impact of how well these reactors operate is considerable, since in the petroleum sector alone the annual processing capacity for various hydrotreatments (such as desulfurization, hydrocracking, metals removal, denitrification, and so on) exceeds billions of metric tons (Trambouze, 1991; Al-Dahhan et al., 1997; Duduković et al., 1999). With the permanent market shift towards increasing demand for light oil products (naphtha, middle distillates, gas oil), and the decreasing need for heavy cuts, it is forecast that the refiners will keep improving their "bottom-of-the-barrel" processing units for upgrading heavy oil and residual feedstocks (Trambouze, 1993; Meyers, 1996). In addition, to comply with the EPA/EU low sulfur emission policy by the 2005 deadline, considerable pressure is put on the oil refining industries to produce diesel with low sulfur content (Marcandelli et al., 2000).

When liquids containing low concentrations of *fine* solid impurities are treated in packed beds, clogging develops so that ultimately the flow becomes severely hampered. A classical practical example arises in the area of deep bed filtration (DBF) of hydrosols where wastewater is treated by trapping solid biological materials to yield purified water. A less common area where this phenomenon represents a serious concern is in hydrotreating and hydrocracking of resids where oil-borne *nonfilterable* fines, such as native clay or incipient coke, are incriminated in the drop of catalytic reaction performances, and in the triggering of reactor hydrodynamic instabilities. The fines in such *nonaqueous* media can be of different origins. They may naturally occur in the liquid feed; a good example is the clay-containing Athabasca oil sands bitumen (Chan et al., 1994; Narayan et al., 1997). They may also be produced *in situ* in the form of coke (Wang et al., 1999,

Correspondence concerning this article should be addressed to F. Larachi.
Current address of S. Roy: Corning Inc., Modeling and Simulation, SP_TD_01_2, Corning, NY 14831.

2001) such as in the reduced-crude hydrodesulfurization process (Meyers, 1996) as a result of the decomposition and condensation of heavy asphaltic compounds. Other possibilities include the presence of iron sulfides produced by corrosion reactions in upstream equipment (Koyama et al., 1995). In the case of bitumen, the particles are usually small ($< 20\ \mu$m) and cannot be retained in the upstream filtration trains. They subsequently enter the catalytic reactor and get progressively deposited upon the packing that makes up the reactor bed. Current industry response is to leave the bed collecting fines until the pressure drop climbs to a critical value forcing reactor shutdown (Gray et al., 2002). Then, the reactor is emptied and reloaded afresh with pristine catalyst. Since in chemical terms, the catalyst is still highly active, such a drastic remedy causes considerable profit loss of the process. An alternative riposte consists in using catalyst pellets having special surface design for providing the necessary catalytic activity along with the suitable geometry to cope with the adhesion of unfilterable fines. For the time being, such geometry profiling is more an art science. The CDS-NP macaroni catalyst series of UOP RCD Unionfining process is a good example of that art (Meyers, 1996). Unfortunately, such solutions remain palliative in nature in the sense that they cannot get rid completely of bed clogging.

New fundamental knowledge is required to tackle the complex hydrodynamics and surface phenomena involved in the clogging with fines of packed-bed reactors typical of the oil industry. Indeed, there is a lack of descriptive and quantitative models which can be used for planning strategies for minimizing the problem of clogging in these reactors. This contribution is offered as a step in that direction.

In this work, a computational fluid dynamics (CFD) based approach is developed for describing the deposition of fines in packed beds. Our endeavor at calculating two-dimensional (2-D) axisymmetrical unsteady-state filtration concentrates in formulating the appropriate drag closures and the effective specific surface area model. For the time being, the proposed CFD framework is intended to provide a qualitative/quantitative assessment of the impact of fines buildup during *single-phase* flow hydrodynamics. Such impact is measured in terms of pressure drop as a function of specific deposit relationships, as well as in terms of the clogging patterns developing throughout the porous medium. The approach is benchmarked using the experiments and observations of Narayan et al. (1997), who studied the macroscopic dynamics of kerosene/carbon black fine/glass bead bed flows. The set of mass and momentum conservation PDE equations is solved using the CFDLIB code (Kashiwa et al., 1994).

Our approach rests on formulating the problem in the following manner:

- Ensemble-averaged continuity equations (mass conservation) for both fluid and packed bed
- Ensemble-averaged momentum conservation equations for the fluid phase
- Ensemble-averaged species balance equation for the fines
- Closure equations needed for the filtration rate and the momentum exchange term
- Phenomenological description of fines capture
- Model for the effective specific surface area
- Bed voidage distribution model.

Table 1. Experimental Filtration Conditions Simulated in CFD (Narayan et al., 1997)

Properties of Materials
Liquid
Kerosene:
Viscosity; 2.14 mPa·s
Density; 784.3 kg/m^3
Re = 0.1; 0.5, 1
Fines
Carbon black
Diameter; 5–10 μm, 8 μm average
Density; 1,768 kg/m^3
Influent concentration; 100–200 mg/L
Packing Material
Glass spheres
Density; 2,487 kg/m^3
Diameter; 1.0×10^{-3} m
Porosity; 0.37
Hamaker constant for glass-carbon-kerosene 3.04×10^{-20} J
Geometry of the Packed-Bed Reactor
Diameter; 2.54 cm
Height; 30 cm

Experimental Data Used for Model Validation

Validation of the model for the fines capture, the clogging of bed, and the buildup in the pressure gradient is based on the experimental work of Narayan et al. (1997). Ambient clogging tests (room temperature and atmospheric pressure) were run in a one inch-I.D. and one ft-high packed tube. A nonaqueous liquid (kerosene), seeded with various concentrations of 8-μm carbon black mimicking-fines, flows upwards across a porous layer of randomly dumped one-mm glass beads (henceforth, referred to as "the collectors"). See Table 1 for the other experimental conditions.

It was found in the experiments that the liquid superficial velocity was a key factor in controlling the amount of deposition, as well as the morphology, of the deposits of fines. The lower the liquid throughputs, the higher the collection rates of fines, and, correspondingly, the larger the rise in pressure drops.

Visual inspection of the evolving morphology of the aggregates anchored to the collectors is indicative of complex capture mechanisms. Mainly driven by fine-fine interceptions, scattered and loose flocs (or cotton-like clusters) form at low liquid velocities. Especially at lower liquid feed rates, the fines preferentially deposit adjacent to the contact points between collectors, presumably because these are sites of static holdup of liquid with lower rates of fluid renewal. At high liquid feed rates, collector-fine (and very likely non-Brownian) interactions occur, presumably through fluid drag, gravity-buoyancy, and London-van der Waals forces, to yield disparate scattered thin patches of fine deposits over the collector outer surface.

The objective of this work is to present a flow simulation of the liquid/fines/porous medium system in the laboratory conditions of Narayan et al. (1997), and to compare the computational results with experimental observations presented in terms of pressure drop rise as a function of volume-averaged bed specific deposit relationships. This effort highlights the possibilities, as well as the limitations, of the multiphase flow simulations using CFD of the flows relevant to the

petroleum refining area involving filtration mechanisms. It is hoped that this will arouse interest and new ideas for future improvements to the theory and the computational approach of deep bed filtration (DBF).

Governing Equations for the Fluid Transport in Porous Medium

An Euler-Euler two-fluid, 2-D, unsteady-state CFD model is formulated to describe the space-time evolution of clogging by fines and the resulting buildup of pressure drop in DBF as a function of the average specific deposit. The application problems targeted are typical of the petroleum refining catalytic processes. Specifically, the packing material and the fines dealt with here fall within the mm and the 10 μm ranges, respectively, with fines' loadings well below 0.2% v/v.

To conduct the multiphase flow simulations in DBF, use is made of the Los Alamos CFDLIB multiphase flow simulation library (Padial et al., 2000; Kashiwa and Rauenzahn, 1994). The ensemble-averaged Euler *k*-fluid multimaterial formalism is used to integrate over finite control volumes (or grid cells) representing the computational grid, the time-dependent *phasic* conservation equations. For details about the CFDLIB numerical schemes, several references from the Los Alamos group can be consulted (Padial et al., 2000; Brackbill et al., 1997; Kashiwa and Rauenzahn, 1994; Kashiwa et al., 1994).

Here, the nonaqueous liquid/fine/porous medium multiphase system representing the DBF problem is treated as a system of two interpenetrating continuum phases: (a) a *dilute* fluid phase consisting of the liquid embracing fines present at yet tiny volume fractions in the incoming stream; (b) and a pseudo-continuous solid phase made up of the packing particles (called "collectors" for the purposes of this work) of the porous bed along with the fines being attached to their surface due to capture. Both phases within each finite control volume of the computational domain are assumed to have complementary ensemble-averaged volume fractions which, due to clogging by fines, evolve in time. To ensure resolution and convergence, the grid cells should be specified of such a size to be sufficiently small in comparison of the dimensions of the DBF-containing vessel in order to assume constancy at the cell level of volume fractions, velocity, pressure, or any advected scalar or vector (Kashiwa et al., 1994; Sokolochin and Eigenberger, 1994).

To perform the flow field simulations using CFD, the packed bed was discretized in a r-z framework into cells by assigning at every grid point $\underline{\boldsymbol{a}}$ in the computational domain, a cell volume $v(\underline{\boldsymbol{a}})$ and an initial local porosity $\epsilon_o(\underline{\boldsymbol{a}})$.

The following assumptions are inherent in the formulation presented in this article.

- The properties of the pseudo-homogeneous fluid, that is, liquid + fines, referred to as *fluid*, are equal to those of the embracing liquid (inlet fines volume fraction $\leq 0.1\%$).
- The density of the packing is not affected by the collected mass of fines, that is, dilute solid phase.
- The single homogeneous fluid is assumed to be isothermal and incompressible.
- Turbulent transport neglected, that is, Reynolds stress negligible.
- Net sink for fluid momentum due to fines capture on the collector neglected.
- No re-entrainment of deposited fines occur,
- Bed clogging by *sieving* effect (Tien and Payatakes, 1979) and *blocking mode* (Choo and Tien, 1995a) does not occur.
- The local fluid velocity in every grid cell is below the critical velocity that impedes deposition due to a large drag force acting on the impinging fines. For hydrosols, this critical velocity lies within the 1–20 mm/s range (Rege and Fogler, 1988; Mackie et al., 1987); (this assumption is checked *post facto*).
- The coupling between the fluid and solid phases is monitored via the *fines* filter equation (Eq. 8) and the interaction drag or momentum exchange force term (Eq. 20).
- The conservation equations of mass, momentum, and species (that is, the fines) are provided in the form of the Euler-Euler formulation. These equations consist of the continuity and the Navier-Stokes equations for the fluid phase, a continuity equation for the solid *stationary* phase, and a species balance equation for the fines being displaced from the fluid phase to the solid phase.

The continuity equation for the fluid phase is

$$\frac{\partial}{\partial t}\epsilon\rho_\ell + \nabla\bullet\epsilon\rho_\ell\underline{\boldsymbol{u}}_\ell + \rho_f N = 0 \tag{1}$$

The continuity equation for the solid phase is

$$\frac{\partial}{\partial t}(1-\epsilon)\rho_s = \rho_f N \tag{2}$$

The species balance equation for the fines is

$$\frac{\partial}{\partial t}\epsilon c + \nabla\bullet\epsilon c\underline{\boldsymbol{u}}_\ell + N = 0 \tag{3}$$

The momentum balance equation for the fluid phase

$$\frac{\partial}{\partial t}\epsilon\rho_\ell\underline{\boldsymbol{u}}_\ell + \nabla\bullet\epsilon\rho_\ell\underline{\boldsymbol{u}}_\ell\otimes\underline{\boldsymbol{u}}_\ell = -\epsilon\nabla P + \epsilon\rho_\ell\underline{\boldsymbol{g}} + \nabla\bullet\mu_\ell\epsilon\left(\nabla\underline{\boldsymbol{u}}_\ell + [\nabla\underline{\boldsymbol{u}}_\ell]^T\right) + \underline{\boldsymbol{F}}_{\ell s} \tag{4}$$

The solid (packing) phase transfers momentum with the fluid phase through the effective drag term. While in the fluid phase this results in modifying the velocity field, in the packing phase it results in shear stress and interparticle compressive stress. The solids stress balance is not explicitly solved here, since the scope of our work focuses on the fluid phase and the way fines get deposited *on* the packing.

The fines are imposed in the influent stream as a fluid step-increase function after *suddenly* switching from the *steady-state* flow of clean or "fines-free" liquid flow through the immaculate porous medium. The solution of this initial state is obtained by solving the continuity and the momentum balance equations for the pure liquid case.

The continuity equation for the liquid phase is

$$\nabla\bullet\epsilon_o\rho_\ell\underline{\boldsymbol{u}}_\ell^o = 0 \tag{5}$$

Momentum balance equation for the liquid phase

$$\frac{\partial}{\partial t}\epsilon_o \rho_\ell \underline{\boldsymbol{u}}^o_\ell + \nabla\bullet \epsilon_o \rho_\ell \underline{\boldsymbol{u}}^o_\ell \otimes \underline{u}^o_\ell = -\epsilon_o \underline{\nabla} P + \epsilon_o \rho_\ell \underline{\boldsymbol{g}} + \nabla\bullet \mu_\ell \epsilon \left(\nabla \underline{\boldsymbol{u}}^o_\ell + \left[\nabla \underline{\boldsymbol{u}}^o_\ell\right]^T\right) + \underline{\boldsymbol{F}}^o_{\ell s} \quad (6)$$

The problem depicted by the above five *scalar* conservation equations (Eqs. 1–4) is 2-D + t. It contains five natural unknowns: ϵ, c, P, and the $\underline{\boldsymbol{u}}_\ell$ axial and radial scalar projections. It further contains two dependent unknowns: the filtration rate and the momentum exchange term. These require additional closure formulations. The procurement of expressions of the dependent unknowns as a function of some of the five natural unknowns permits to have a closed form of the CFD model yielding a solution specific to the present hydrodynamic flow problem.

Closure Models

Ad hoc closure models are required for the filtration rate N and the momentum exchange term in the conservation equations Eqs. 1–6.

Filtration rate

The filtration (or deposition) rate determines the degree of collection of fines. On a volume basis, it measures the volume of fines collected per unit grid cell volume and unit time. The filtration rate is related to the specific deposit σ which represents the volume of fines deposited per unit grid cell volume. Both N and σ are *local* and time-dependent. Hence, N is assumed to depend on the local number of fines present in the fluid, that is, the fines concentration c, and the local state of the porous medium that is characterized by the specific deposit (Tien, 1989)

$$N(\sigma, c, t, \underline{\boldsymbol{a}}) = \frac{\partial \sigma}{\partial t} \quad (7)$$

For a microscopic description required in the CFD approach, it is useful to recast the *unidirectional* macroscopic phenomenological formalism that ties the fines concentration and the fluid velocity to the filtration rate. This is achieved by assuming that at the grid cell level, the relationship is symbolically preserved so that the filtration rate is proportional to the local concentration and interstitial fluid velocity. In the absence of more sophisticated "local" models, we tailor the well-trodden and popular logarithmic law of Iwasaki (1937) to express such a dependence of the deposition rate

$$N = \lambda c \,\|\, \underline{\boldsymbol{u}}_\ell \,\| \quad (8)$$

where λ is the filter coefficient which can be thought of as the probability for a fine to be captured as it travels a unit distance through the bed (Tien, 1989). The form of the filter coefficient is dictated by the nature of the capture phenomena in play, and by the amount of capture as bed clogging proceeds.

The fines deposition, hence, evolves through two stages (Choo and Tien, 1995a):

- The first stage describes the initial, almost clean filter bed, having an initial filter coefficient λ_0, and a specific deposit $\sigma \approx 0$ (Figure 1a). During this stage, the fines adhere individually as a *monolayer* on the collector surface through fine-collector interactions. In the vicinity of the collector, their capture is an outcome of a force balance which determines their motion. In the present analysis, Brownian diffusion ($d_f > 1\ \mu$m), electrostatic, and double-layer forces are neglected. Furthermore, as is typical in hydrosol filtration at tiny feed rates, the inertial forces of the fines are marginal. Hence, the forces likely in play are the fluid drag, and the London van der Waals surface-interactive force. As long as the monolayer keeps developing, the specific deposit obeys the condition

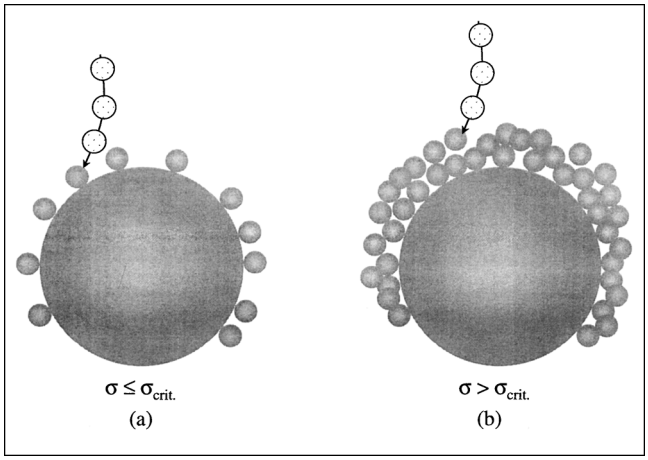

Figure 1. Deposition of fines on collectors: (a) initial stage, monolayer (fine-collector interaction); (b) second stage, multiple-layer (fine-fine interaction).

$$\sigma \le \sigma_{\text{crit}} \quad (9)$$

which is derived assuming a layer thickness equal to that of one fine diameter. The critical specific deposit σ_{crit} corresponds to the amount of fines required for completing a monolayer having a coating porosity ϵ_d. Its full expression will be given later in Eq. 37.

Under these circumstances, the trajectory simulations of Rajagopalan and Tien (1976) yield the following numerical correlation for the initial filter coefficient

$$\lambda(\underline{\boldsymbol{a}}) = \lambda_o(\underline{\boldsymbol{a}}) = \frac{9}{4d_c} A_s\left(1-\epsilon_o(\underline{\boldsymbol{a}})\right) N_R^2 \left[\frac{2}{3} N_L^{1/8} N_R^{-1/8} + \frac{9}{4000} N_G^{6/5} N_R^{-12/5}\right] \quad (10)$$

where A_s is the Happel parameter defined as

$$A_s = \frac{2\left(1-p^5\right)}{w} \quad (11)$$

$$p = \sqrt[3]{1-\epsilon_o(\underline{\boldsymbol{a}})} \quad (12)$$

$$w = 2 - 3p + 3p^5 - 2p^6 \quad (13)$$

The dimensionless groups representing the relative importance of gravitational and viscous forces N_G, the relative importance of the London-van der Waals forces, and the viscous forces N_L and the interception parameter N_R are defined respectively, as

$$N_G(t, \underline{a}) = \frac{(\rho_f - \rho) d_f^2 g}{18\pi\mu \| \underline{u}_\ell \|} \tag{14}$$

$$N_L(t, \underline{a}) = \frac{4H}{9\pi\mu d_f^2 \| \underline{u}_\ell \|} \tag{15}$$

$$N_R = \frac{d_f}{d_{co}} \tag{16}$$

• During the second stage, no room is left for adhesion of the fines through the fine-collector interactions and the condition given by Eq. 9 no longer holds. Driven now by fine-fine interactions, an interception mechanism is established, and the fines start piling up as a multilayer deposit (Figure 1b). The fines already deposited on the collectors themselves become secondary collectors: the capture can be viewed as an autocatalytic process in which the filtration rate gets accelerated as more and more fines are trapped. The filter coefficient no longer remains constant with time and an expression representing its time-evolution during the second stage is necessary. Several empirical correlations are available in literature, wherein the filter coefficients during ripening have to be fitted to the experimental filtration rate data (O'Melia and Ali, 1978; Chiang and Tien, 1985; Vigneswaran and Tien, 1987; Mackie et al., 1987). For the sake of preserving a predictive capability to the present approach, we preferred to use the numerical correlation derived from trajectory analyses of Choo and Tien (1995a) as a function of the interception number, the specific deposit, and the initial filter coefficient

$$\frac{\lambda(t, \underline{a})}{\lambda_o(\underline{a})} = (1-Y)\left[1 + \frac{0.6794}{1-\epsilon_o(\underline{a})}\left(\frac{1}{N_R} - 0.921\right)\left(\frac{\sigma(t, \underline{a})}{1-\epsilon_d}\right) + \frac{0.1731}{(1-\epsilon_o(\underline{a}))^2}\left(\frac{1}{N_R^2} + \frac{3}{N_R} - 117.1\right)\left(\frac{\sigma(t, \underline{a})}{1-\epsilon_d}\right)^2\right] + Y\left[1 + 9.61(1-\epsilon_o(\underline{a}))^{2/3}\left(\frac{\sigma(t, \underline{a})}{1-\epsilon_d}\right)\right] \tag{17}$$

where

$$Y = \frac{0.598 k_d^{-0.8}(1-\epsilon_o(\underline{a}))^{-2}\left(1 + \frac{0.0128}{N_R}\right)\left(\frac{\sigma(t, \underline{a})}{5(1-\epsilon_d)}\right)^{1.63 + \frac{5.5\times10^{-4}}{N_R}}}{1 + 0.598 k_d^{-0.8}(1-\epsilon_o(\underline{a}))^{-2}\left(1 + \frac{0.0128}{N_R}\right)\left(\frac{\sigma(t, \underline{a})}{5(1-\epsilon_d)}\right)^{1.63 + \frac{5.5\times10^{-4}}{N_R}}} \tag{18}$$

In Eqs. 17 and 18, the deposit permeability k_d was estimated using a Kozeny-Carman like expression (Dullien, 1992), and the porosity of the deposit ϵ_d was assigned a value of ca. 0.8 (Tien, 1989).

Momentum exchange

In any given point $\underline{a}$ of the computational domain, the momentum exchange vector can be formulated as the product of the volume fractions of the two k phases, the momentum exchange rate coefficient, $X_{\ell s}$, and the local relative velocity between the k phases (Kashiwa et al., 1994)

$$\underline{F}_{\ell s} = -\epsilon(1-\epsilon) X_{\ell s} \underline{u}_\ell \tag{19}$$

in which $X_{\ell s}$ takes the general *creeping flow* form as a function of the local instantaneous values of the porosity and of the effective specific surface area $\bar{a}_{\beta\gamma}$ (to be discussed later)

$$X_{\ell s}(t, \underline{a}) = h_K a_{\beta\gamma}^{-2}(t, \underline{a}) \frac{(1-\epsilon(t, \underline{a}))}{\epsilon^3(t, \underline{a})} \mu_\ell \tag{20}$$

In clean bed simulations, $X_{\ell s}$ takes the following simplified form

$$X_{\ell s}(\underline{a}) = \frac{36 h_K}{d_{co}^2} \frac{(1-\epsilon_o(\underline{a}))}{\epsilon_o^3(\underline{a})} \mu_\ell \tag{21}$$

In combination with Darcy's law, $X_{\ell s}$ can easily be interpreted using the permeability concept

$$X_{\ell s}(t, \underline{a}) = \frac{\mu_\ell}{B(t, \underline{a})[1-\epsilon(t, \underline{a})]} \tag{22}$$

with the local permeability being defined as

$$B = \frac{\epsilon^3(t, \underline{a})}{h_K \bar{a}_{\beta\gamma}^2(t, \underline{a})[1-\epsilon(t, \underline{a})]^2} \tag{23}$$

Note that the Blake-Kozeny-Carman constant h_K in Eqs. 20, 21 and 23 is assigned a mean value equal 5 as a consensus value in DBF (O'Melia and Ali, 1978; Stephan and Chase, 2000).

As suggested from Eq. 23, the drop in local permeability with time is caused by two factors: a drop in local porosity as the specific deposit increases, and at the same time, an increase in local effective specific surface area as a result of the increasing number of fines being attached to the collectors

(Herzig et al., 1970). A trade-off between the "bulk" effect due to porosity deflation, and the "areal" effect due to the enhancement of the liquid-solid interface for drag by the fines will be assessed later.

Neglect of the previous areal effect would yield the following simplified form of the momentum exchange coefficient

$$X_{\ell s}(t, \underline{a}) = \frac{36h_K}{d_c^2(t, \underline{a})} \frac{[1-\epsilon(t, \underline{a})]}{\epsilon^3(t, \underline{a})} \mu_\ell \qquad (24)$$

As will be seen, such formulation fails to forecast the rise of pressure drop in clogged beds because the impact of the specific surface area is essentially overlooked. As drag models based on porosity changes are expected not to produce satisfactory predictions of the pressure drop build-up (O'Melia and Ali, 1978), the impact of the rise in effective specific surface area is included. For that purpose, an accurate model of the effective specific surface area must be developed and included in the momentum exchange coefficient given by Eq. 20.

Effective specific surface area model for momentum transfer

With the progress of bed clogging, the solid-fluid surface area of the *filter bed* is altered by two opposing phenomena (Stephan and Chase, 2000). The capture of fines by the collector causes an increase in the surface area by an amount equivalent to the cross-section fraction γ being actually exposed by the *anchored* fines to the streamline flow (Figure 2a). *Ipso facto*, a fraction of the *collector* area located immediately beneath the anchored fine no longer contributes to the subsequent collection events. This last phenomenon, known as the "shadow effect" (Tien and Payatakes, 1979), results from the spontaneous hindrance occasioned by the tethered fines, and also from the alteration by the fine of the local flow field; both impede access to the collector area A_Δ behind the fine for further interceptions (Figure 2a).

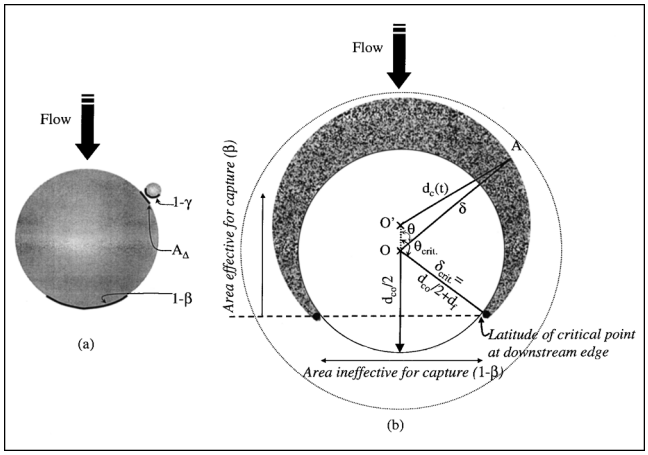

Figure 2. (a) Shadow effect, cross-sectional fractions of fine and collector; (b) sphere-in-cells fines layer building up on top of collector for estimating the cross-section fraction β of collector.

Consequently, in terms of solid-fluid drag activity, not all the total solid-fluid *geometrical* surface area participates in the momentum transfer during the subsequent collisional interceptions occurring at the periphery of the collecting assemblage, that is, collector-deposited fines. Due to peculiarities in the geometrical configuration of the collector-deposited fines porous medium, such as throats, cul-de-sacs, rough relief, creeks, and so on, only a fraction of the total surface area, henceforth referred to as the *effective specific surface area*, $\bar{a}_{\beta\gamma}$, is involved in the interception and also in the momentum exchange coefficient of the drag term appearing in the momentum balance equation (Eqs. 4 and 20).

At every point $\underline{a}$ of the computational domain, the *instantaneous* effective specific surface area, expressed per unit *total solid volume in grid cell*, can be summarized in the following compact relationship

$$\bar{a}_{\beta\gamma}(t, \underline{a}) = \frac{\overbrace{\tilde{N}_c(\underline{a})\beta(t, \underline{a})\pi d_c^2(t, \underline{a})}^{\text{Useful area of collectors}} + \overbrace{\tilde{N}_c(\underline{a})\partial\tilde{N}_f(t, \underline{a})\left[\gamma\pi d_f^2 - A\Delta(t, \underline{a})\right]}^{\text{Peripheral area due to captured fines}}}{\tilde{N}_c(\underline{a})\frac{\pi}{6}d_{co}^3 + \tilde{N}_f(t, \underline{a})\frac{\pi}{6(1-\epsilon_d)}d_f^3} \qquad (25)$$

Similarly, the ability the collector has to capture the incoming fines largely depends on the location of impact on the collector periphery. While frontal locations, especially on the upstream collector pole, are likely to be active in the capture process, points such as those located on the collector downstream pole are more or less passive. To handle this angular feature, it can be stated that the collector offers a cross-section fraction β for fines capture (Figure 2a).

The cross-section fractions β and γ are thus measures of the peripheral areas effectively involved in interception. They account for the surface of the target reachable by the incoming fines and fluid for momentum and mass transfers. For instance, a cross-section fraction of 0.5 means that interception fully exploits the frontal hemispheric area of the target (Stephen and Chase, 2000).

in which $\tilde{N}_c(\underline{a})$ and $\tilde{N}_f(t, \underline{a})$ are, respectively, the number of collectors, and the number of captured fines in cell volume $\upsilon(\underline{a})$; $\partial\tilde{N}_f(t, \underline{a})$ represents how many fines, per collector, culminate at the periphery of the collecting assemblage at time t. d_{co} and d_c are the diameters of, respectively, the initial *clean* collector and the *dirty* collector in duty at time t; and ϵ_d is the porosity of the fines deposit usually assigned a value of *ca*. 0.8 (Tien, 1989).

The number of collectors in any given cell located at $\underline{a}$ can be obtained straightforwardly as

$$\tilde{N}_c(\underline{a}) = \frac{6\upsilon(\underline{a})}{\pi d_{co}^3}[1-\epsilon_o(\underline{a})] \qquad (26)$$

Analogously, the number of fines deposited within the time period $[0 - t]$ in cell $\upsilon(\underline{a})$ is computed from the variation of the solid volume fraction caused by deposition

$$\tilde{N}_f(t, \underline{a}) = \frac{6\upsilon(\underline{a})}{\pi d_f^3}\left[\epsilon_o(\underline{a}) - \epsilon(t, \underline{a})\right](1 - \epsilon_d) \qquad (27)$$

Or, equivalently, in terms of the local value of the specific deposit

$$\sigma(t, \underline{a}) = \left[\epsilon_o(\underline{a}) - \epsilon(t, \underline{a})\right](1 - \epsilon_d) \qquad (28)$$

As time evolves, a deposit layer develops on top of the collector. Accordingly, the collector diameter swells and the collector center drifts upwards from O to O′ (Figure 2b). Usually, the *crescent-like* deposited layer is at its thickest at the front stagnant point of the collector (Choo and Tien, 1995b). To account for the nonuniform circumferential growth of the deposit, the increase in the collector diameter in every cell of the flow field is calculated as a function of the specific deposit assuming sphere-in-cell model configurations such as that of Choo and Tien (1995b) illustrated in Figure 2b

$$d_c(t, \underline{a}) = d_{co}\sqrt[3]{1 + \frac{\sigma(t, \underline{a})}{(1 - \epsilon_d)\left[1 - \epsilon_o(\underline{a})\right]}} \qquad (29)$$

The collector area loss A_Δ occasioned by the shadow effect per attached fine is estimated from the shadow left by an equilateral triangle in which the fine is inscribed, as shown in Figure 3

$$A_\Delta(t, \underline{a}) = \frac{\pi d_c^2(t, \underline{a})}{2}\left[-1 + \sqrt{1 + \frac{3d_f^2}{d_c^2(t, \underline{a})}}\right]\cos\frac{\sqrt{3}\,d_f}{d_c(t, \underline{a})} \qquad (30)$$

As argued earlier, the peripheral fines culminating over the collecting assemblage populate the area corresponding to the cross-section fraction β. The number of peripheral fines becomes thus (Vigneswaran and Tulachan, 1988)

$$\partial\tilde{N}_f(t, \underline{a}) = 4\beta(t, \underline{a})(1 - \epsilon_d)\left(\frac{d_c(t, \underline{a})}{d_f}\right)^2 \qquad (31)$$

For the effective specific surface area given by Eq. 25 to be fully computable, it is necessary now to estimate the cross-section parameters β and γ.

When $\sigma \approx \sigma_{\text{crit}}$ (Eq. 9, Figure 1a), it is safe to assume that an upper bound of the cross-section fraction corresponds to the hemispheric frontal area of the anchored fine. This situation holds during the first stage on the initial almost clean filter bed. Thus, we have approximately

$$\gamma = 0.5 \qquad (32)$$

During the subsequent stage when multiple layers of fines form on top of the collector, the impinging fines encounter a roughened relief. Hence, interception, rather than being on a one-to-one basis, most likely involves boundaries of several fines at a time (Figure 4). It appears at this stage that a rigorous geometrical model for fines capture through fine-fine interactions is an overkill, given the other uncertainties in the formulation that may mask any improved geometric model. As also pointed out by Stephen and Chase (2000), a γ value as given by Eq. 32 proves inadequate. As suggested by Figure 4, the cross-section parameter γ is expected to change with the evolution of the specific deposit. Instead and for simplifi-

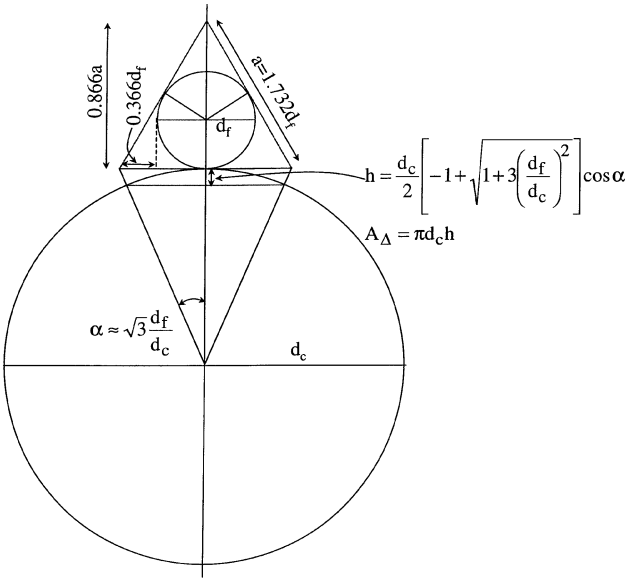

Figure 3. Geometry of the shadow area hidden by the fine on top of the collector.

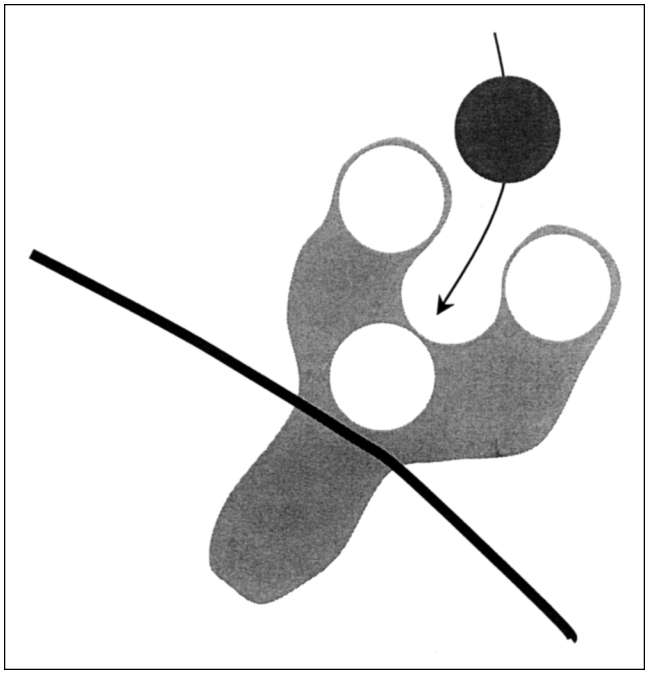

Figure 4. Representative capture of an impinging fine via multiple interactions with anchored fines.

cation purposes, the model is allowed to search for a single *overall* γ value within the range [0.5 − 1] until an acceptable match between measured and predicted pressure drops across the bed vs. the current value of specific deposit is achieved for every Reynolds number value. As the CFD simulations are time-consuming, we did not attempt to precisely locate the optimum value of γ. Hence, when the specific deposit exceeds the critical specific deposit σ_{crit}, that is, Eq. 9 is not satisfied, the recommended value for the conditions of this work fall within the range

$$\gamma \approx 0.6 \text{ to } 0.75 \tag{33}$$

On the other hand, the cross-section parameter for the collector β is evaluated assuming that the growth of the fines layer around the collector can be described by the aforementioned sphere-in-cell model sketched in Figure 2b. Taken at a snapshot for a given azimuthal coordinate θ, the distance between the center O of the clean collector and a peripheral point A on the fines mantle is approximated by (Choo and Tien, 1995b)

$$\delta \approx \frac{d_{co}}{2}\sqrt{1+2h_o}\left[1+\frac{h_o\cos\theta}{\sqrt{1+2h_o}}+\frac{h_o^2\cos\theta}{2(1+2h_o)}\right] \tag{34}$$

where

$$h_o = \frac{d_c(t)}{d_{co}} - 1$$

Physically, the *downstream* edge of the deposit layer is delineated by a ring accommodating a string of fines of diameter d_f girdling the collector (two filled black circles, Figure 2b). In a 2-D view (Figure 2b), the critical point of deposition (δ_{crit}, $\theta_{\text{crit.}}$) is restricted by the sphere of the lowest volume in which a fine can fit, that is, ($\delta_{\text{crit.}} = d_{co}/2 + d_f$. Hence, it is postulated that the collector area beneath the *latitude* of this critical point is hidden and unavailable for interception, whereas the area upstream allows for capture and growth of the fines layer. As time evolves, the latitude of the ring slides downwards due to the thickening of the deposit. Consequently, the cross-section fraction is expected to increase accordingly.

Knowing the value of σ at $\underline{a}$ and instant t yields from Eq. 29 the diameter $d_c(t)$. By equating δ with δ_{crit} in Eq. 34, one obtains through an iterative procedure the angle θ_{crit} of the critical point of deposition. Geometrical arguments yield the area of the hidden pole of the collector

$$A_H \approx \frac{\pi}{2} d_{co}^2 (1+\cos\theta_{\text{crit}}) \tag{35}$$

Finally, the cross-section fraction β is obtained from the ratio of the hidden pole area to that of the collector area with the diameter d_c calculated by means of Eq. 29

$$\beta = 1 - \frac{A_H}{\pi d_c^2(t)} \tag{36}$$

Owing to the angular dependence of the fines coating thickness illustrated above, the critical specific deposit must be evaluated after resting the passive area of the downstream collector's pole. Hence, instead of using the smooth-layer coating relationship of Tien and Payatakes (1979), the following relationship, derived from simple geometrical arguments, must be used for ensuring the switch from the filter coefficient λ_o Eq. 10 to the filter coefficient λ Eq. 17

$$\sigma_{\text{crit}} \approx \frac{3}{2}\frac{d_f}{d_{co}}\left[1-\epsilon_o(\underline{a})\right](1-\epsilon_d)(1-\cos\theta_{\text{crit}})^2(2+\cos\theta_{\text{crit}}) \tag{37}$$

Numerical Simulation of Narayan et al. (1997) Filtration Experiments

Voidage model of the clean packed bed

The high aspect ratios $d_R/d_c \approx 25$ and $H/d_R \approx 12$ yielding in our case *ca.* 175,000 particles in the bed makes computeri-

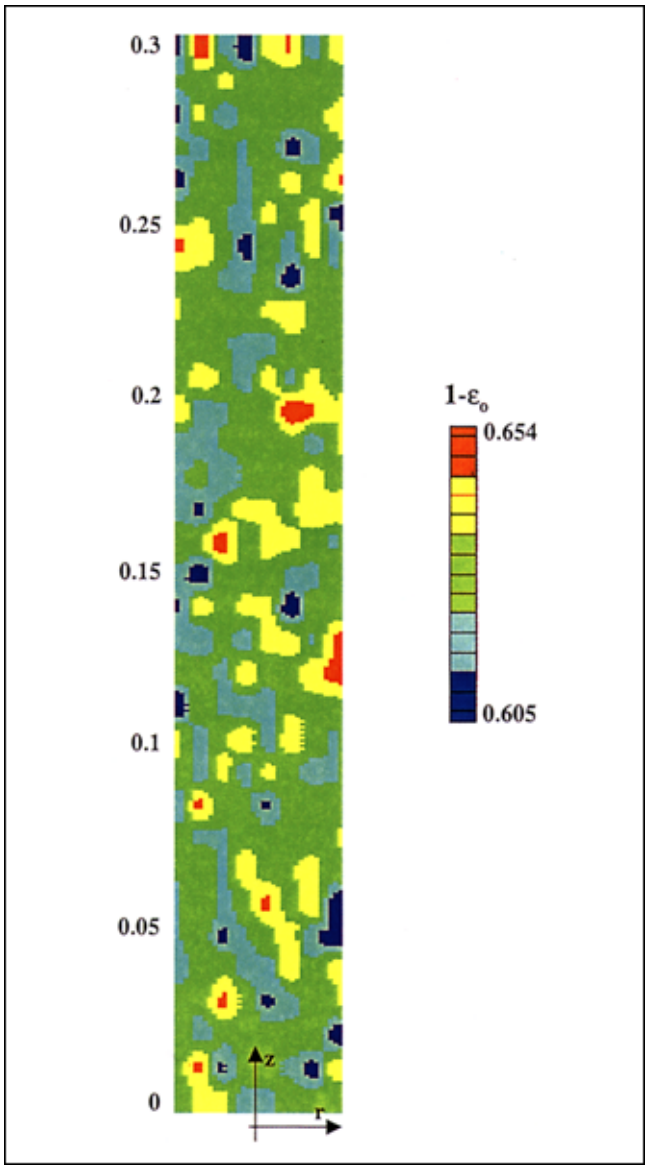

Figure 5. Initial solid volume fraction r-z distribution of the clean packed bed.

zation of the porous medium geometry impossible. The k-fluid Euler approaches are suitable to lift such a limitation by viewing voxels in the computational domain as made up of *probabilistic volume fraction* contributions arising from each phase occupying the voxel, but without requiring detailed knowledge of local geometry. Note that in this description (see, for example, Drew (1983) and Drew and Passman (1998)) the identity of an individual particle is lost and each phase is treated as a pseudo-continuum in each cell and in the whole domain. The forces arising from the interactions between the phases (both "skin" and "form" drag) are modeled with appropriate closures, as discussed above, with the understanding that the conservation equations themselves (of the k-fluid model) are exact. The validity of the closures and their exactness is justified with arguments as those made above, and, in any case, must satisfy the *post-facto* test in being able to explain the macroscopic experimental data.

A voidage field, or, equivalently, its complementary solid-filled counterpart, is thus generated in a 2-D axisymmetrical computational domain of communicating grid cells to represent the initial porosity of the clean packed bed state. The dimensions of the bed are summarized in Table 1. Once the mesh size is decided, the local voidage per cell is obtained by means of a simple simulation program that assigns randomly porosity values by using a normal Gaussian probability density function (Jiang et al., 2001; Chen et al., 2001). A mean bed porosity of 0.37 is used, which is the value measured by Narayan et al. (1997) for their bed. Also, the allowed disparities in porosity varied within the range 0.346−0.395. The obtained voidage field is shown in Figure 5 as a contour plot of solid volume fraction for a discretization using 2,768 cells.

Mesh, boundary and initial conditions

Due to the simple cylindrical bed geometry, a single-block computational mesh of a structured type is used in the CFDLIB finite volume solver with explicit temporal differencing (Brackbill et al., 1997). The Eulerian boundary conditions for the fluid (or liquid) are of four types: specified inflow, conserving outflow, centerline symmetry, and reflective-wall (or free-slip wall) condition.

The fluid (or liquid, clean bed simulation) is fed upwards through an already *imbibed* bed. At the inlet boundary, CFDLIB requires that the fluid velocity and the fines concentration be specified. To prevent slow convergence, the inflow *liquid* velocity profile is ramped from zero to its final

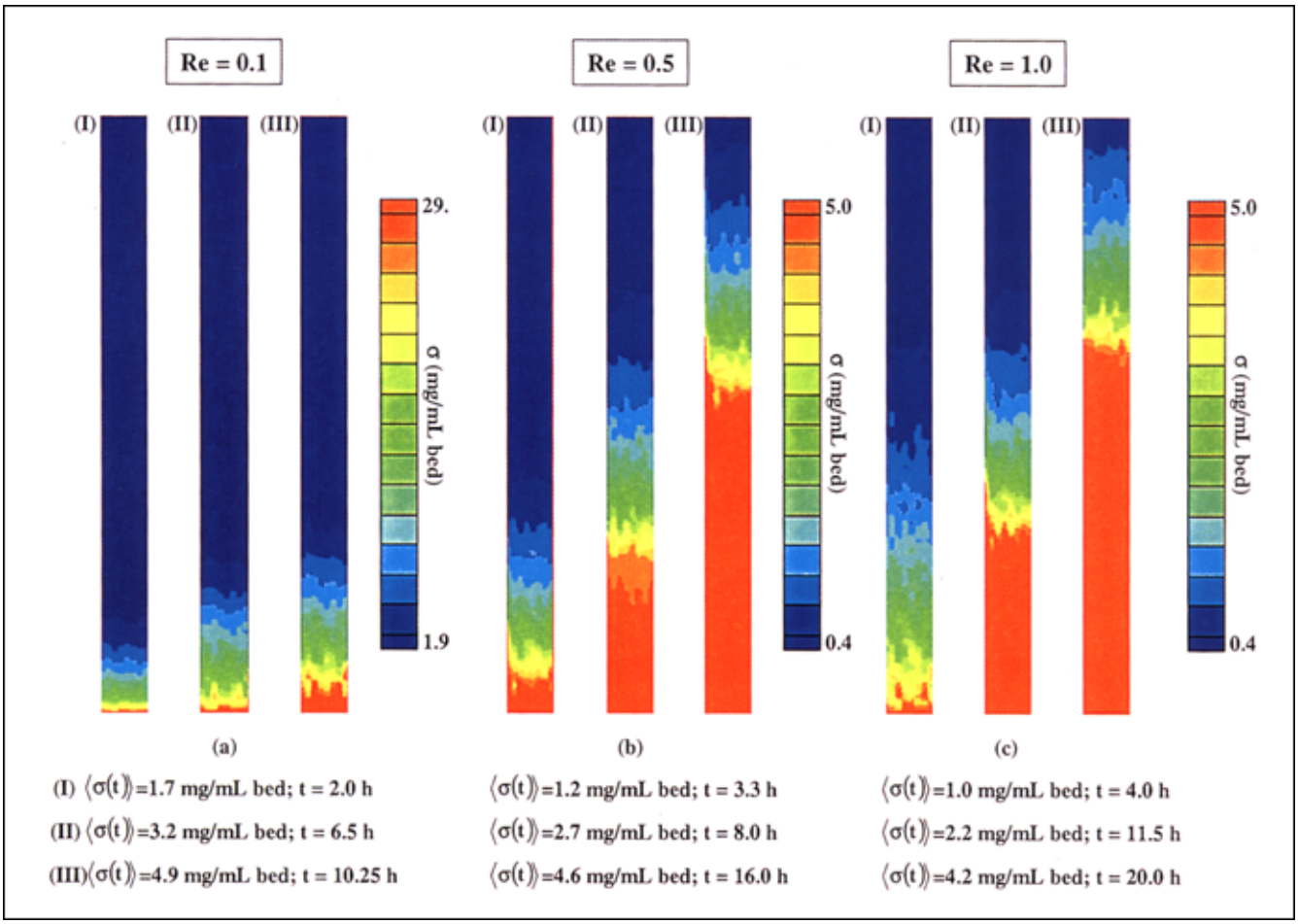

Figure 6. Contours at various clogging times of specific deposit contour plots at different liquid Reynolds numbers.

Snapshots taken at an approximately constant mean global specific deposit in the bed. Influent concentration $c_o = 142$ mg/L.

value which is reached within about 10 *real-time* seconds. At the bed top, the outflow boundary condition is computed to ensure mass conservation of the fluid (or liquid). At the vessel vertical boundaries, a free-slip wall condition is imposed. This means that the velocity component or the flux of an advected scalar (fines concentration) normal to the wall is zero. Also, the wall tangential velocity component is approximated by that of the adjacent cell-centered cell.

Transient simulations of *clean* bed liquid flow are run until the flow field (pressure and velocity) reaches steady state. Under these circumstances, the conservation equations (Eqs. 5 and 6) are solved in the absence of fines in the liquid along with the momentum exchange coefficient calculated using the Blake-Kozeny-Carman drag Eq. 21. Transient simulations with fines-containing liquid are then resumed by solving Eqs. 1–4. The clogging simulations correspond to sets of experiments reported by Narayan et al. (1997) for three kerosene Reynolds numbers: $Re = 0.1$, 0.5, and 1.

To ensure grid convergence, numerical simulations are performed on computational grids of up to 3,000 cells. The finer grid was chosen to allow: (a) representative collectors-per-cell statistics, (b) realistic execution cpu time, and (c) converging results. The coarser grid was set once the mismatch between results from fine and coarse grids becomes significant. When the pressure drop vs. specific deposit profiles at different grid resolutions yield mean absolute relative errors $< 0.5\%$ (and residuals' standard deviation $< 0.3\%$), grid independence was assumed to be attained. Because the simulations are computationally intensive, the grid size is held to a minimum, and, the smaller the Reynolds number, the finer the grid. The dense character of the selected computational grids and the smallness of the time steps preclude the occurrence of problems associated with numerical diffusion. Simulations are carried out on a dual-processor Pentium III running at 1,000 MHz each. Typical simulation time is about 3 CPU days for simulating clogging flows lasting up to 20 real-time hours at $Re = 0.1$ and 2,768 grid cells.

With the above CFD model of DBF, the evolution of clogging in the packed bed can be simulated. Hence, detailed numerical output results can be obtained including the time-evolving fields of porosity, specific deposit, velocity, permeability, and pressure. Also, the instantaneous bed scale or bulk

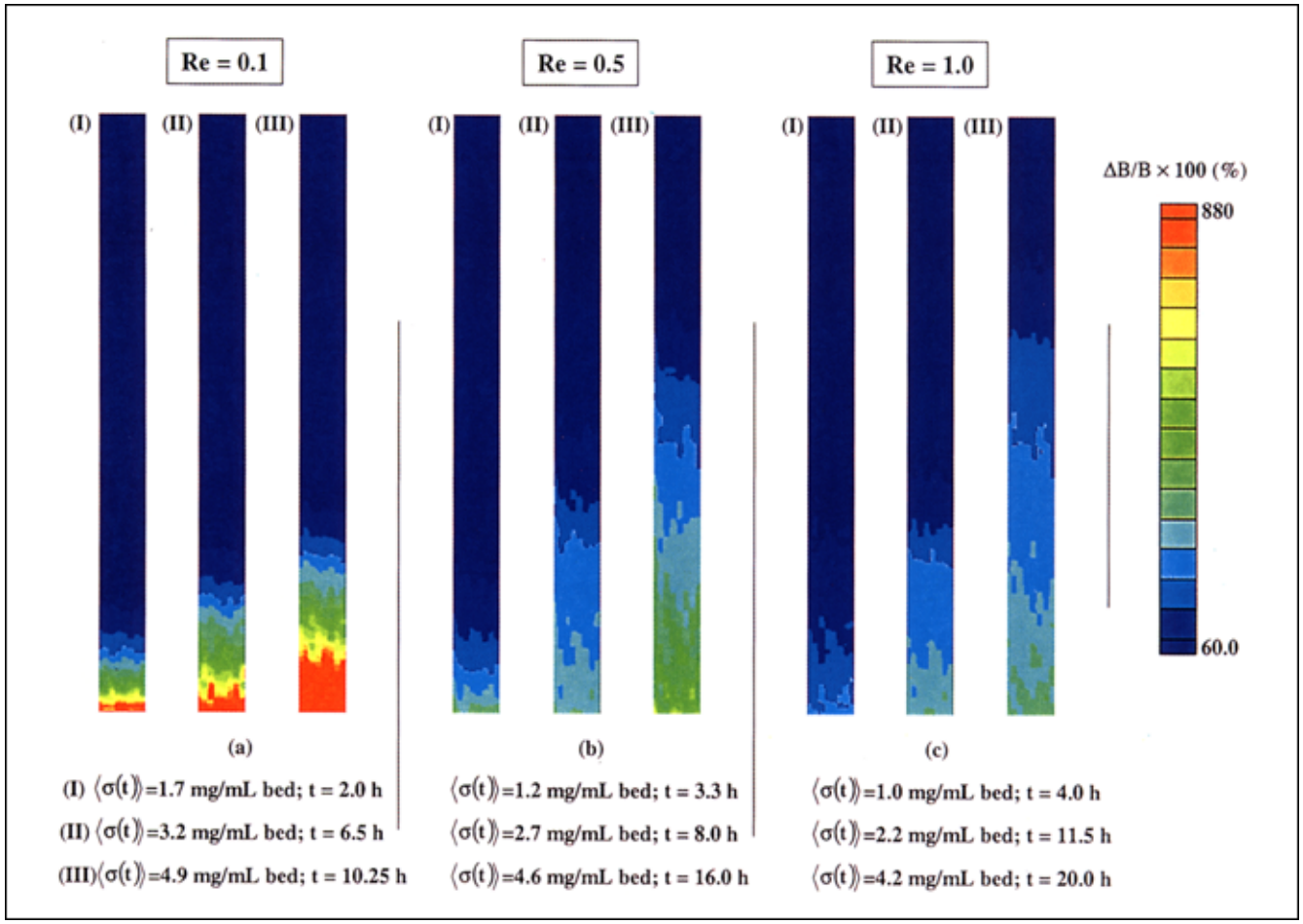

Figure 7. Contours at various clogging times of the local permeability drop off expressed as $100 \times [B_o - B(t)]/B(t)$ with respect to the initial clean bed state permeability field. The snapshots correspond to the same conditions as in Figure 6.

The permeability deviation is evaluated at every grid cell center in the computational grid.

pressure drop, defined as the difference between the inlet and outlet pressures divided by the bed height, can be calculated and plotted against the mean global specific deposit. Note that the mean global specific deposit is the volume averaged specific deposit over all the computational grid cells which is calculated as

$$\langle \sigma(t) \rangle = \frac{\sum_i \sum_j \sigma_{ij}(t, \underline{a}) v_{ij}(\underline{a})}{\sum_i \sum_j v_{ij}(\underline{a})} \tag{38}$$

Discussion and Concluding Remarks

To illustrate the qualitative and quantitative filtration features, the simulated results are presented in terms of contour plot snapshots of specific deposit, local permeability, and local porosity for the kerosene Reynolds numbers of 0.1, 0.5 and 1. Likelihood of the simulated patterns is supported from comparing bulk simulated solutions with bulk experimental measurements of the pressure drop buildup vs. global specific deposit.

With filtration phenomena in porous media being a complex problem, noninvasive field probing of the transient phenomena accompanying fluid flow and fines deposition in the bed is not trivial even by performing the most sophisticated laboratory sensing or imaging techniques. One of the advantages CFD simulations permit is the possibility to mimic these phenomena by solving the rigorous transport equations.

The axisymmetrical contour plot of the local specific deposit (Eq. 28) is illustrated in Figures 6a–6c for, respectively, $Re = 0.1$, 0.5, and 1.0. Three snapshots (I)–(III) are shown for each Re number value. The snapshot triplets (I), or (II) or (III) correspond to approximately constant mean global specific deposit in the bed (Eq. 38), *ca*. 1.3, 2.7, and 4.6 mg fines/mL bed, respectively.

Coherent with the photographs of Narayan et al. (1997), the bed increasingly captures fines of the lower Reynolds numbers (or the liquid throughput). The peak specific deposits of 30 mg/mL occur at $Re = 0.1$ (Figure 6a), which are up to a factor six larger than the peak specific deposits at Re

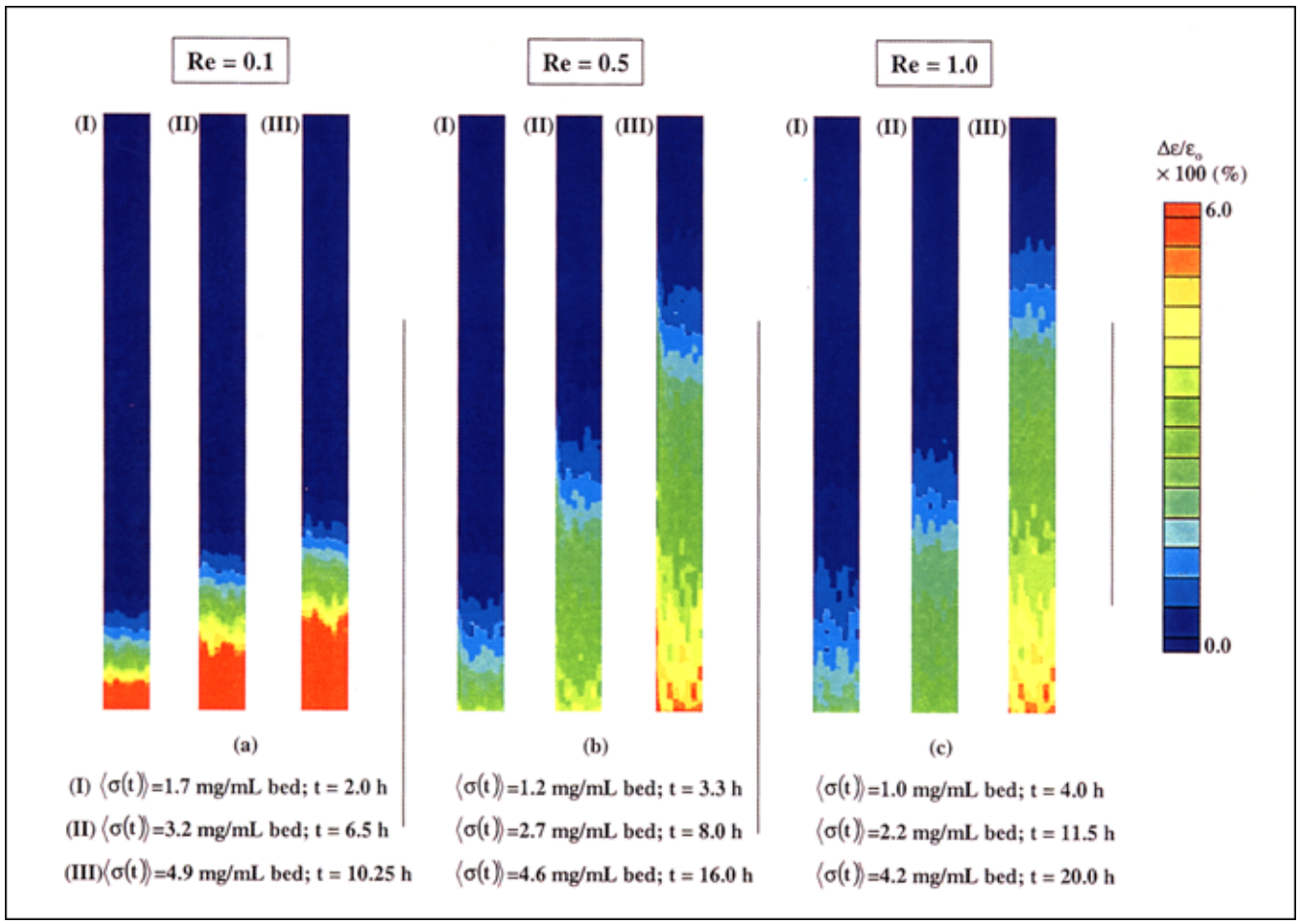

Figure 8. Contours at various clogging times of the local porosity drop off expressed as $100 \times (\epsilon_o - \epsilon(t))/\epsilon_o$ with respect to the initial clean bed state porosity field.

The snapshots correspond to the same conditions as in Figure 6. The porosity deviation is evaluated at every grid cell center in the computational grid.

= 0.5 or 1.0 (Figures 6b and c). As time evolves, the *clogging front* progressively fills up the column. However, clogging is more confined in the entrance region at low *Re* numbers. Hence, the bed undergoes more inhomogeneous clogging with the lower Reynolds numbers yielding sharper contrasts in the specific deposits between the entrance and the exit regions. Moreover, longer clogging duration is required, as expected, to attain the same global specific deposit with increasing *Re* number.

The drop in local bed permeability for the same simulation conditions is illustrated in Figures 7a–7c. The contour plot snapshots are depicted using as a measure of divergence from the clean bed state the error function $100\times[B_o - B(t)]/B(t)$. This function measures how much the instantaneous local permeability B (Eq. 23) departs, during the course of clogging, from the permeability B_o of the immaculate bed. It is important to note that the lower scale value at 60% in Figure 7 has been set for commodity to better illustrate the color contrast so that permeability changes between 0 and 60% are embedded in this lower limit.

The simulated permeability patterns are in qualitative agreement with those corresponding to a specific deposit. At the lowest Reynolds value, the bed entrance portion, that is, the area of the highest collection *activity*, undergoes permeability drop off by almost one order of magnitude (red spot in Figure 7a). There, the permeability falls by 882% with respect to the clean bed local permeability, B_o. In the upper bed portions, deposition has less a hold and the clean bed permeability is preserved as the bed outlet is approached, that is, $B \rightarrow B_o$. However, with the increase in DBF time or global specific deposit, the *contaminated* bed fraction swells up. As the *Re* number is increased and for constant global specific deposit values, the reduction in permeability is distributed in a more homogeneous manner throughout the bed (Figures 7b and 7c). This result is in agreement with the Narayan et al. (1997) experimental observations who found that deposition was distributed more evenly throughout the bed. For the highest *Re* and the highest global specific deposit, bed local permeabilities decrease by a factor of three or less.

It is very instructive to parallel the behavior in permeability with that exhibited in the porosity field for the same conditions. Hence, Figures 8a–8c depict snapshot contour plots of the local void volume fraction taken at the conditions of Figures 6 and 7. The plots are constructed using as a measure of departure from the initial local porosity, the error function $100\times[\epsilon_o - \epsilon(t)]/\epsilon_o$. This function was also evaluated at global scale, using the global specific deposit and the average bed porosity (see Table 2).

Table 2. Evolution of Global Porosity Change as a Function of Global Specific Deposit

Re	0.1			0.5			1.0		
$\langle\sigma(t)\rangle^*$	1.7	3.2	4.9	1.2	2.7	4.6	1.0	2.2	4.2
$D\ (\%)^{**}$	1.4	2.4	3.7	0.9	2.0	3.6	0.9	1.7	3.2

* mg fines/mL bed

** $D\ (\%) = 100\times\dfrac{\langle\sigma(t)\rangle}{\rho_f\langle\epsilon_o\rangle(1-\epsilon_d)}$

While local bed permeability may decline by up to an order of magnitude, the corresponding local porosity does not change by more than 6% (red spots in Figure 8a). Reduction in local porosity is less pronounced at higher *Re* numbers. On a bed averaged scale, the decrease in the average bed porosity never exceeds 3.7% (Table 2) for the highest global specific deposits.

The maximum change in local permeability due to the bulk effect in Eq. 23, that is, via $\epsilon^3/(1-\epsilon)^2$, does not exceed 35% for the maximum increase by 6% in the local porosity (Figures 8a–8c). Consequently, the bulk effect alone is not able to explain why the permeability diminishes by up to 880%

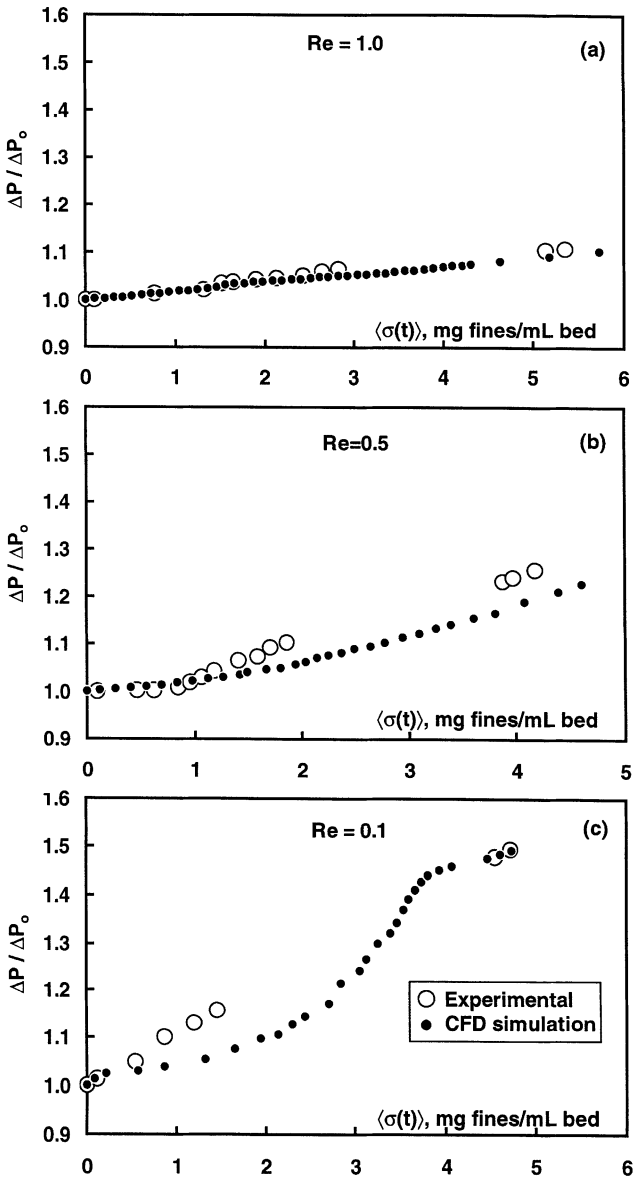

Figure 9. Increase in pressure drop with mean global specific deposit at Reynolds numbers of (a) 1.0, (b) 0.5, (c), 0.1.

Experimental data of Narayan et al. (1997), CFDLIB simulation using the momentum exchange coefficient (Eq. 23) referred to as the Kozeny drag model. Influent concentration $c_o = 142$ mg/L.

(Figures 7a–7c). It is therefore the areal effect contributed in Eq. 23 by the effective specific surface area, that is, via $\bar{a}_{\beta\gamma}$, that contributes for the majority of the changes undergone by the permeability. This result is not surprising, in view of the experimental results from researchers like Herzig et al. (1970), O'Melia and Ali (1978), and Vigneswaran and Tulachan (1988) to propose macroscopic empirical drag models accounting for the fines buildup. The present work corroborates such findings and stresses out their importance at a more local scale. The variable bringing about the most important changes in permeability is the effective specific surface area which required an accurate model such as the one proposed earlier (Eq. 25).

The agreement with the bulk experimental measurements is in general very conclusive for the global pressure drop vs. the global specific deposit (Figures 9a–9c). The measured pressure drops at $Re = 1.0$ are predicted very well by the CFD-DBF approach. At lower Re number of 0.5, the model slightly underpredicts the pressure drop for higher global specific deposits. One likely interpretation could be the increasing manifestation of liquid dead zones forming around the collectors' contact points. Such regions, acting as collection systems, narrow the useful area for flow and favor the accumulation of fines (see Narayan et al. (1997) photographs) which yield an increase in pressure drop which is not handled in the present model formulation. At the smallest Re value, the predictions are close to the measured pressure drops in the early and late DBF instances. Although the simulated profile exhibits a sigmoid shape in the intermediate $\langle \sigma(t) \rangle$ range, it is not experimentally evident. Such peculiar numerical behavior can be ascribed to the effective specific surface area model which underpredicts the impact of the collecting assemblages, that is, fines + collector, on the drag force when the specific deposits become large. There, the cross-section fractions γ and β (Eqs. 32, 33, and 36) intervening in Eq. 25 would require more sophisticated model formulations. It can also be due to the simplifications in the model regarding the dead zone collecting regions.

Acknowledgments

The authors thank the following institutions for their financial contributions: The Natural Sciences and Engineering Research Council of Canada, the Fonds pour la formation de chercheurs et d'aide à la recherche (Québec). The Los Alamos National Laboratory is also acknowledged for giving us access to the CFDLIB library of codes. A. O. would like to thank the financial support from CONACyT, Mexico and the Universidad Autonoma de Tlaxcala, Mexico.

Notation

A_H = hidden area in downstream collector pole, m^2
A_s = Happel constant
A_Δ = shadow area, m^2
$\underline{a}$ = grid point representing a cell center in computational grid
$\bar{a}_{\beta\gamma}$ = effective specific surface area, m^{-1}
B = local bed permeability, m^2
c = fine volumetric concentration (liquid volume basis)
d = particulate diameter (collector or fine), m
$\underline{F}_{\ell s}$ = momentum exchange force, Pa/m
$\underline{g}$ = gravitational acceleration, m/s^2
H = Hamaker constant, J
h_K = Blake-Kozeny-Carman constant
k_d = deposit permeability, m^2
N = filtration rate (reactor volume basis), s^{-1}
$\tilde{N}_c$ = number of collector in grid cell volume v
$\tilde{N}_f$ = number of trapped fines in grid cell volume v
$\partial\tilde{N}_f$ = number of peripheral fines per collector
N_G = gravitational dimensionless group
N_L = London-van der Waals dimensionless group
N_R = interception dimensionless group
P = pressure, Pa
p = Happel cell parameter
Re = Reynolds group, $\rho U d_c/\mu$
r = radial coordinate, m
t = time, h
U = fluid superficial velocity, m/s
$\underline{u}_\ell$ = velocity, m/s
v = grid cell volume, m^3
w = Happel cell parameter
X = momentum exchange rate coefficient, kg/m^3/s
Y = parameter in Eq. 17
z = longitudinal coordinate, m

Greek letters

β = collector cross-section fraction
γ = fine cross-section fraction
δ = distance from clean collector center to coating border, m
ϵ = grid cell porosity
λ = filter coefficient, m^{-1}
μ = density, Pa·s
ρ = density, kg/m^3
σ = specific deposit (reactor volume basis)
$\langle \sigma \rangle$ = bed volume-averaged specific deposit

Subscripts and superscripts

c = collector
crit = critical
d = deposit
f = fine
ℓ = liquid
o = clean bed state
s = solid

Literature Cited

Al-Dahhan, M. H., F. Larachi, M. P. Duduković, and A. Laurent, "High-Pressure Trickle Bed Reactors—A Review," *Ind. Eng. Chem. Res.*, **36**, 3292 (1997).

Brackbill, J. U., N. L. Johnson, B. A. Kashiwa, and W. B. VanderHeyden, "Multiphase Flows and Particle Methods," CFD Ann. Conf. of Comput. Fluid Dynamics Soc. of Canada, Univ. of Victoria, Victoria, BC, Canada (May 28–29, 1997).

Chan, E. W., K. H. Chung, M. Veljković, and J. K Liu, "Hydrodynamics and Fines Capture in Packed Bed Hydrotreaters," *Can. Conf. Chem. Eng.*, Ottawa, Canada (Oct. 1994).

Chen, J. W., N. Radoš, M. H. Al-Dahhan, M. P. Duduković, D. Nguyen, and C. Parimi, "Particle Motion in Packed/Ebullated Beds by CT and CARPT," *AIChE J.*, **47**, 994 (2001).

Chiang, H., and C. Tien, "Dynamics of Deep Bed Filtration. Part I: Analysis of Two Limiting Situations," *AIChE J.*, **31**, 1349 (1985).

Choo, C-u., and C. Tien, "Simulation of Hydrosol Deposition in Granular Media," **41**, 1426 (1995a).

Choo, C-u., and C. Tien, "Analysis of the Transient Behavior of Deep-Bed Filtration," *J. Colloid Interface Sci.*, **169**, 13 (1995b).

Drew, D. A., "Mathematical Modeling of Two-Phase Flow," *Ann. Rev. Fluid Mech.*, **15**, 261 (1983).

Drew, D. A., and S. L. Passman, *Theory of Multicomponent Fluids (Applied Mathematical Science)*, Vol. 135, Springer-Verlag, New York (1998).

Duduković, M. P., F. Larachi, and P. L. Mills, "Multiphase Reactors —Revisited," *Chem. Eng. Sci.*, **54**, 1975 (1999).

Dullien, F. A. L., *Porous Media Fluid Transport and Pore Structure*, 2nd ed., Academic Press, San Diego (1992).

Gray, M. R., N. Srinivasan, and J. H. Masliyah, "Pressure Buildup in Gas-Liquid Flow Through Packed Beds Due to Deposition of Fine Particles," *Can. J. Chem. Eng.*, in press (2002).

Herzig, J. P., D. M. Leclerc, and P. Le Goff, "Flow of Suspensions

through Porous Media, Application to deep bed filtration," *Ind. Eng. Chem.*, **62**, 8 (1970).
Iwasaki, T., "Some Notes on Sand Filtration," *J. Amer. Water Works Assoc.*, **29**, 1591 (1937).
Jiang, Y., M. H. Al-Dahhan, and M. P. Duduković, "Statistical Characterization of Macroscale Multiphase Flow Structures in Trickle Beds," *Chem. Eng. Sci.*, **56**, 1647 (2001).
Kashiwa, B. A., N. T. Padial, R. M. Rauenzahn, and W. B. VanderHeyden, "A Cell-Centered ICE Method for Multiphase Flow Simulations," *ASME Symp. on Numerical Methods in Multiphase Flows*, Lake Tahoe, NV, FED-vol. 185 (1994).
Kashiwa, B. A., and R. M. Rauenzahn, "A Multimaterial Formalism," *ASME Symp. on Numerical Methods in Multiphase Flows*, Lake Tahoe, NV, FED-vol. 185 (1994).
Koyama, H., E. Nagai, H. Torri, and H. Kumagai, "Japanese Refiner Solver Problems in Resid Desulfurization Unit," *Oil & Gas J.*, **93**, 8290 (1995).
Mackie, R. I., R. M. W. Horner, and R. J. Jarvis, "Dynamic Modeling of Deep-Bed Filtration," *AIChE J.*, **33**, 1761 (1987).
Marcandelli, C., A. S. Lamine, J. R. Bernard, and G. Wild, "Liquid Distribution in Trickle-Bed Reactors," *Oil & Gas Sci. & Technol.*, **55**, 407 (2000).
Meyers, R. A., *Handbook of Petroleum Refining Processes*, 2nd ed., McGraw-Hill, New York (1996).
Narayan, R., J. R. Coury, J. H. Masliyah, and M. R. Gray, "Particle Capture and Plugging in Packed-Bed Reactors," *Ind. Eng. Chem. Res.*, **36**, 4620 (1997).
O'Melia, C. R., and W. Ali, "The Role of Retained Particles in Deep Bed Filtration," *Prog. Wat. Tech.*, **10**, 167 (1978).
Padial, N. T., W. B. VanderHeyden, R. M. Rauenzahn, and S. L. Yarbro, "Three-Dimensional Simulation of a Three-Phase Draft-Tube Bubble Column," *Chem. Eng. Sci.*, **55**, 3261 (2000).
Rajagopalan, R., and C. Tien, "Trajectory Analysis of Deep Bed Filtration with the Sphere-in-Cell Porous Media Model," *AIChE J.*, **22**, 523 (1976).
Rege, S. D., and H. S. Fogler, "A Network Model for Deep Bed Filtration of Solid Particles and Emulsion Drops," *AIChE J.*, **34**, 1761 (1988).
Sokolichin, A., and G. Eigenberger, "Gas-Liquid Flow in Bubble Columns and Loop Reactors: Part I: Detailed Modeling and Numerical Simulation," *Chem. Eng. Sci.*, **49**, 5735 (1994).
Stephan, E. A., and G. G. Chase, "Development of Volume-Average Theory for Deep-Bed Filtration," *AIChE J.*, **46**, 1918 (2000).
Tien, C., and A. C. Payatakes, "Advances in Deep Bed Filtration," *AIChE J.*, **25**, 737 (1979).
Tien, C., *Granular Filtration of Aerosols and Hydrosols*, Butterworths-Heinemann, Boston (1989).
Tien, C., "Hydrosol Deposition in Porous Media: The Effect of Surface Interactions," *Advance Powder Technol.*, **11**, 9 (2000).
Trambouze, P., "Multiphase Catalytic Reactors in the Oil Industry, an Introduction," *Rev. Inst. Franç. Pétr.*, **46**, 433 (1991).
Trambouze, P., "Engineering of Hydrotreating Processes," *Chemical Reactor Technology for Environmentally Safe Reactors and Products*, NATO Ser. E, Applied Sciences, H. I. De Lasa, G. Dogu, A. Ravella, eds., p. 425 (1993).
Vigneswaran, S., and R. V. Tulachan, "Mathematical Modeling of Transient Behaviour of Deep Bed Filtration," *Wat. Res.*, **22**, 1093 (1988).
Vigneswaran, S., and C. Tien, "Transient Behavior of Deep-Bed Filtration of Brownian Particles," *Chem. Eng. Sci.*, **42**, 2729 (1987).
Wang, S., K. H. Chung, J. H. Masliyah, and M. R. Gray, "Deposition of Fine Particles in Packed Beds at Hydrotreating Conditions: Role of Surface Chemistry," *Ind. Eng. Chem. Res.*, **38**, 4878 (1999).
Wang, S., K. H. Chung, and M. R. Gray, "Role of Hydrotreating Products in Deposition of Fine Particles in Reactors," *Fuel*, **80**, 1079 (2001).

Manuscript received Sept. 7, 2001, and revision received Feb. 4, 2002.